ARTICLE

Reversible sorption of carbon dioxide in Ca-Mg-Fe systems for thermochemical energy storage applications

Lucie Desage,[a] Terry D. Humphries,*[a] Mark Paskevicius [a] and Craig E. Buckley [a]

Alternatives to fossil fuels are necessary to reduce greenhouse gas emissions, and energy storage is crucial to transition to renewable energy. Thermochemical energy storage is one option to store energy for 24/7 utilisation, and as such, the reversible carbonation of the Ca:Mg:Fe oxide system was investigated to determine its feasibility as a thermochemical energy storage material. The Ca:Mg:Fe (1:1:1) sample synthesised from co-crystallisation of metal acetates retained reversible CO_2 sorption at 90% over 100 cycles, thus the associated physical properties were thoroughly investigated. Powder X-ray diffraction analyses indicated the formation of dicalcium ferrite and magnesioferrite, respectively in the decarbonated and carbonated states, which suggested a synergistic effect enhancing the reversible sorption of CO_2 in the $2CaO \cdot Fe_2O_3 \cdot MgO$ intermediate system involved in the reaction mechanism. The thermodynamics of the reactions were determined using pressure-composition-isotherm measurements, resulting in calculated enthalpies and entropies of ΔH_{abs} = −146 ± 5 kJ.mol^{-1} and ΔS_{abs} = −141 ± 5 J.mol^{-1}.K^{-1}, and ΔH_{des} = 178 ± 4 kJ.mol^{-1} and ΔS_{des} = 167 ± 4 J.mol^{-1}.K^{-1} for CO_2 absorption and desorption, respectively. The application of the Kissinger method determined an activation energy of 203 ± 14 kJ.mol^{-1} for the decarbonation reaction. The maximum energy storage density of the system was evaluated to be 468 kJ.kg^{-1} with an operating temperature of ≈ 750 °C. Overall, the Ca-Mg-Fe system can integrate thermochemical batteries and is promising to promote thermochemical energy storage for backing up power production using renewables.

.

Introduction

The anthropogenic emission of greenhouse gases originating mainly from burning fossil fuels is causing disastrous climate change and endangering the survival of the Earth's ecosystems.[1] As stated in the Paris agreement in 2015, the world must urgently ban fossil fuels to limit global warming to 1.5 °C.[2] Failing to do so will have dramatic consequences leading to irreversible damage.[3]

To eradicate the use of fossil fuels, energy storage is essential to promote the development and utilisation of renewable resources, such as solar and wind.[4] For example, concentrated solar power (CSP) plants require large-scale energy storage systems operating at high temperatures (400 – 1000 °C) to achieve grid flexibility and reliability as base-load power production facilities.[5] Thermal energy storage (TES) and more specifically, thermochemical energy storage (TCES) systems, accommodate the requirement of high operating temperatures and low-cost to allow these systems to be efficiently combined with renewable power production plants.[6] TCES relates to materials that undergo reversible endo- and exothermic gas

sorption reactions, allowing for the storage of thermal energy and its release in the form of heat, respectively, as defined by eq. 1 where M is an alkaline-earth metal.[7] Particularly, cheap and abundant calcium carbonate operates at 900 °C and has high energy density (~1.7 MJ.kg^{-1}).[7-10] For example, a 100 MW CSP plant would require ~6250 t of $CaCO_3$, considering 40% efficiency, to back up the power production for 12 h.

$$MCO_3 + \Delta H \rightleftharpoons MO + CO_2 \qquad (1)$$

Beyond application in CSP plants, TCES using metal carbonates can be implemented into thermochemical batteries (TCB) at smaller scales to run heat-to-power engines.[7] A recent study highlighted the challenges associated with the high operating temperatures (< 900 °C) of calcium carbonate, especially concerning engineering aspects and longevity of storage capacity.[11] The bimetallic carbonate, dolomite ($CaMg(CO_3)_2$), operates at lower temperatures (< 600 °C) and also has potential for TCES applications.[12] Humphries *et al.* demonstrated the reversible carbonation of the magnesium carbonate member of dolomite using additives such as molten salts.[12] At high temperature, the presence of inert MgO in the dolomite matrix seems to prevent sintering and pore plugging over multiple carbonations of the calcium carbonate member, although cyclic capacity diminishes over time.[13, 14]

Recent studies have demonstrated that the addition of Fe and Mn can enhance the cycling capacity and stability of calcium carbonate based systems.[15-17] Bai *et al.* used natural dolomite

precursors treated with acid and addition of Mn and Fe to form Ca/Mg:Mn:Fe composites with the aim of improving the optical absorbance for direct solar applications.[15] Interestingly, natural crystal structures containing Mg, Mn and Fe are known.[18, 19] Dolomites are ancient sedimentary rocks characterised by an ordered calcite structure (rhombohedral, $R\bar{3}c$) with an equimolar incorporation of Mg in some of the cationic layers.[20] The substitution of Mg cations with Fe cations is naturally common, forming ferroan dolomites Ca(Mg,Fe)(CO$_3$)$_2$.[19] Specifically, ferroan dolomites with a higher Fe content than Mg are classified as ankerite, which may also contain a small amount of Mn (ferromanganoan).[21]

Extensive thermal analyses of ferroan, ferromanganoan and ankerite dolomites have been carried out in the past century; resulting in differing interpretations of the multistep endothermic events that may correspond to the successive decarbonations of CaCO$_3$, MgCO$_3$ and FeCO$_3$ and of the exothermic events attributed to the formation of different oxides and solid solutions.[18, 19, 22, 23] Specifically, the formation of calcium and magnesium ferrites have been identified.[23] More recently, Ptáček *et al.* updated the literature on the thermal decomposition of ferroan dolomites in varying atmospheres, which confirmed the formation of srebrodolskite (dicalcium ferrite, Ca$_2$Fe$_2$O$_5$) and magnesioferrite (MgFe$_2$O$_4$), and demonstrated the influence of the experimental conditions on the decomposition mechanism and kinetics.[24]

Nevertheless, the study of the re-carbonation and the potential utilisation of natural ferroan dolomites for TCES is lacking. The iron content in natural ferroan dolomites varies depending on the environment of formation and seems to influence the physical properties of the material, notably the decomposition temperature.[18, 25, 26] Various geologic conditions allow for the natural formation of Ca-Mg-Fe ternary carbonates.[18] To understand the processes of formation and substitution of Fe and Mg atoms in the crystal lattice, researchers have studied synthetic ferroan dolomites.[25, 27, 28] To synthesise such compounds, tedious experimental process, requiring extremely high pressure (15 kbar) and relatively high temperature (> 500 °C) have been reported in the literature.[25] Therefore, according to these synthesis conditions, it is unlikely to observe reversible sorption of carbon dioxide in Ca(Mg,Fe)(CO$_3$)$_2$ at the modest process pressures (< 10 bar) and temperatures (< 900 °C) required for TCES applications.

However, the calcium and magnesium ferrites that form during the decomposition of Ca-Mg-Fe ternary carbonates might be interesting for TCES. Ferrites are known for their electrical and magnetic properties, but their range of applications is expanding from biomedical to the energy fields.[29-31] Calcium ferrites have been investigated as catalytic oxygen carriers in redox cycles for hydrogen and syngas production processes via chemical looping.[32-34] Ca$_2$Fe$_2$O$_5$ also demonstrates potential in catalysing CO$_2$ splitting for biofuel production.[35] Recently, Anwar *et al.* obtained promising results using Ca$_2$Fe$_2$O$_5$ as an additive to enhance the conversion and cyclic stability of limestone for TCES.[36]

Initially, this work investigated the potential reversible carbonation of natural ankerite minerals and a milder pathway

to synthesise ankerite-like material. The experimental formation of Ca(Mg,Fe)(CO$_3$)$_2$ was unsuccessful, but the ferrite compounds formed raised interest. Ca-Mg-Fe systems involving calcium and magnesium ferrites in the reversible carbon dioxide sorption of calcium carbonate for TCES have not yet been studied. Thus, this study aims to provide insights into the reaction mechanism taking place, evaluate the performance of Ca-Mg-Fe systems as TCES materials and assess their potential implementation into TCB. Different molar ratios of Ca-Mg-Fe and synthesis pathways have been investigated. In addition, the reversible sorption of carbon dioxide in natural ankerite samples and the various synthesised Ca-Mg-Fe composites over 100 cycles is reported for the first time in the present study. Particularly, the thermodynamics, activation energy and the reaction mechanism of the reversible carbonation of Ca-Mg-Fe (1:1:1) have been determined. The cyclic capacity of each material allowed for the evaluation of their performance and assess their potential utilisation as the energy storage media for TCB.

Experimental

Sample preparation

Samples of natural ankerite were acquired from private mineral collectors and prepared by manually crushing small pieces of the bulk rock with a ceramic pestle and mortar until a fine powder was obtained. The different natural ankerite samples studied are described in Table S1 (ESI).

Artificial Ca-Mg-Fe systems were synthesised using two different synthesis pathways by varying the chemical precursors and their molar ratios. The synthesis methods employed in this study are summarised in Table 1. Samples identification (ID) marked with 'N' were synthesised from calcium nitrate tetrahydrate (Ca(NO$_3$)$_2$.4H$_2$O, Sigma-Aldrich, ACS reagent, 99%), magnesium nitrate hexahydrate (Mg(NO$_3$)$_2$.6H$_2$O, Sigma-Aldrich, ACS reagent, 99%) and iron (II) oxalate dihydrate (Fe(C$_2$O$_4$).2H$_2$O, Sigma-Aldrich, 99%). Samples ID marked with

Table 1. Summary of the synthesis of the samples.

Sample ID	Ca:Mg:Fe molar ratio	Precursors	Synthesis process
CC-N-1:1	1:0:1	Ca(NO$_3$)$_2$.4H$_2$O Mg(NO$_3$)$_2$.6H$_2$O Fe(C$_2$O$_4$).2H$_2$O	Co-crystallisation
CC-N-1:1:1	1:1:1		
CC-AC-1:1:1	1:1:1	Ca(CH$_3$CO$_2$)$_2$.H$_2$O Mg(CH$_3$CO$_2$)$_2$.4H$_2$O Fe(CH$_3$CO$_2$)$_2$	
CC-AC-1:0.5:0.5	1:0.5:0.5		
CC-AC-1:0.3:0.3	1:0.3:0.3		
BM-AC-1:1:1	1:1:1		Ball-milling
CaCO$_3$-Al$_2$O$_3$	-	80 wt.% CaCO$_3$ 20 wt.% Al$_2$O$_3$	

'AC' were synthesised from calcium acetate monohydrate (Ca(CH$_3$CO$_2$)$_2$.H$_2$O, Sigma-Aldrich, ACS reagent, ≥ 99.0%), magnesium acetate tetrahydrate (Mg(CH$_3$CO$_2$)$_2$.4H$_2$O, Sigma-Aldrich, *ReagentPlus*®, ≥ 99%,) and iron (II) acetate (Fe(CH$_3$CO$_2$)$_2$, Sigma-Aldrich, 95%).

For the co-crystallisation synthesis process, the precursors (in their appropriate stoichiometric ratios) were dissolved in Milli-Q water at ambient temperature. The aqueous solution was then dried *in vacuo* using a rotary evaporator at 60 °C. The resulting slurry was dried overnight, at 115 °C for the N samples and 150 °C for the AC samples, in a vacuum oven (Across International) to obtain a dry powder of the co-crystallised precursors.

One of the samples using metal acetates precursors (BM-AC-1:1:1) was prepared directly via ball-milling in an 80 mL stainless steel vial with stainless steel balls (50 balls of 6 mm diameter and 11 balls of 10 mm diameter) in a ball-to-powder ratio of 30:1. The vial was placed in a planetary ball-mill (Fritsch Pulverisette 6, Germany) and rotated at 400 rpm for 1 h.

Following the synthesis process, all samples were dried in a tube furnace under 2 L.min^{-1} of Ar, at 650 °C and 850 °C for the N and AC samples respectively, to form a mixture of oxides. Finally, each sample was carbonated in a silicon carbide reactor cell (Hexoloy, Saint-Gobain, France) under 5 bar of carbon dioxide, while heating from room temperature to 750 °C (~8 °C.min^{-1}).[37, 38]

A sample of CaCO$_3$-Al$_2$O$_3$ (20 wt.%) was also prepared via ball-milling using the protocol described in a previous work (Glen Mills Turbula T2C shaker mixer, 160 rpm, 1 h).[8, 11]

Characterisation

Powder X-ray diffraction

The samples were analysed by powder X-Ray Diffraction (XRD, Bruker D8 Discovery, Co source λ = 1.7890 Å, PSD LynxEye detector) at each subsequent step of the synthesis process and after each experiment using a poly(methylmethacrylate) flat-plate sample holder. Data were acquired over a 2θ range of 10 – 80 °, with a step size of 0.02 ° and count time of 1 s per step. Samples not containing iron were analysed with a Bruker D8 Advance (D8A) diffractometer (Cu source λ = 1. 5406 Å, PSD LynxEye detector) acquiring data in steps of 0.02 ° over a 2θ range of 5 – 80 °. Some samples were analysed by synchrotron powder XRD (SR-XRD) on the Powder Diffraction beamline at the Australian Synchrotron in Melbourne, Australia.[39] The powder samples were loaded in borosilicate capillaries (outer diameter 0.7 mm, wall thickness 0.01 mm) and sealed in air. One-dimensional SR-XRD patterns (monochromatic X-rays with λ = 0.590554(3) Å) were collected using a Mythen microstrip detector with an exposure time of 300 s at two different detector positions at room temperature in order to cover the entire 2θ range (3 – 80 °).[40] Phase identification of the resulting XRD patterns were performed with HighScore Plus (version 3.0.5) using Crystallography Open Database (COD) and Powder Diffraction File (PDF) databases. The composition of the samples was determined by Rietveld refinement using TOPAS.[41] All the fitting curves resulting from the refinements can be found in the ESI, along with the quantitative composition of each sample.

Carbon dioxide sorption

CO$_2$ cycling

The absorption capacity of all samples was measured at 750 °C, over 100 cycles (desorption and absorption), with desorption under vacuum for 1 h and absorption at 5 bar of CO$_2$ (Coregas ≥ 99.995%) for 1 h. All measurements were conducted using a custom-made Sieverts apparatus equipped with a Rosemount 3051S manometer (± 0.035/0 − 55 bar), K-type thermocouple and Pt thermistors.[37] The reference volume was 20.49 cm^3, except for samples CC-N-1:1:1 and CC-AC-1:1:1 which used an apparatus with a reference volume of 19.9 cm^3. The sample of CaCO$_3$-Al$_2$O$_3$ (20 wt.%) was also cycled in these experimental conditions.[11] For each sample, ~0.5 g of material was loaded into a SiC reactor cell with a volume of 47.12 cm^3, except for samples CC-N-1:1:1 and CC-AC-1:1:1 which had a sample cell volume of 38.2 cm^3.[38] The CO$_2$ storage capacity of each sample was calculated using the ratio of the measured capacity at the end of the absorption of each cycle (measured manometrically) over the theoretical maximum CO$_2$ wt.% in the sample determined by quantitative Rietveld refinement of the XRD and SR-XRD data.

Pressure composition isotherms

Pressure Composition Isotherm (PCI) using the Sieverts manometric method were measured on the aforementioned custom-made apparatus with a reference volume of 19.9 cm^3 and a SiC high temperature sample cell (38.2 cm^3).[37] Absorption PCIs of carbon dioxide were measured by increasing the pressure (0 – 12 bar) in steps of ~0.5 bar. Each step lasted until the equilibrium was reached (0.08 wt.% resolution, checked every hour). Similarly, using the same parameters, desorption PCIs were measured by decreasing the pressure in steps of ~0.5 bar. The equation of state for CO$_2$ was used from the NIST Refprop database.[42] 1.08 g of CC-N-1:1:1 was introduced in the reactor cell and the data collected at 4 temperatures (790, 820, 850 and 880 °C) to provide the plateau pressures P_{eq} (bar) for absorption and desorption. Respective van't Hoff plots were drawn according to eq. 2, which allowed for the determination of the thermodynamics of absorption and desorption of CO$_2$ in the Ca-Mg-Fe (1:1:1) system. The reaction enthalpies (ΔH_{des} and ΔH_{abs}) and entropies (ΔS_{des} and ΔS_{abs}) were calculated respectively from the linear slope and intercept of eq. 2 for the desorption and eq. 3 for the absorption, where R is the universal gas constant (8.3145 J.K^{-1}.mol^{-1}).[43]

$$\ln(P_{eq}) = \frac{-\Delta H_{des}}{R}\left(\frac{1}{T}\right) + \frac{\Delta S_{des}}{R} \qquad (2)$$

$$\ln(P_{eq}) = \frac{\Delta H_{abs}}{R}\left(\frac{1}{T}\right) - \frac{\Delta S_{abs}}{R} \qquad (3)$$

Furthermore, a single low pressure absorption measurement (< 1 bar CO$_2$) of CC-N-1:1:1 in the decarbonated state (0.93 g) (after the desorption PCI at 880 °C) was performed using the aforementioned apparatus for 1 h at a constant temperature of 820 °C.

The results of the reversible carbonation cycling performed in a Sieverts apparatus provide information about the material

behaviour that is more representative of a scaled-up system than STA measurements usually presented in TCES materials development studies because of the larger amount of sample.

Simultaneous thermal analysis

Simultaneous Thermal Analysis (STA) was performed using a NETZSCH STA 449 F3 *Jupiter*® apparatus. The instrument was equipped with a Differential Scanning Calorimetry (DSC) sensor and was calibrated using In, Bi, Al, Au and Ag standards, each at 2, 5, 10 and 20 K.min^{-1}. The CO_2 desorption peak of CC-N-1:1:1 was measured while heating ~18 mg of CC-N-1:1:1 in an alumina crucible with a lid (pin-hole) from 40 to 900 °C. The measurements were conducted under a constant Ar flow of 20 mL.min^{-1}. The peak temperature T_p at different heating rates β (2, 5, 10 and 20 K.min^{-1}) was used to draw a Kissinger plot according to eq. 4. The activation energy E_a of the CO_2 desorption was calculated by multiplying the slope of the resulting linear curve by the universal gas constant, R.[44]

$$\ln\left(\frac{\beta}{T_p^2}\right) = \ln\left(\frac{A}{E_a}R\right) - \frac{E_a}{R}\frac{1}{T_p} \tag{4}$$

The STA instrument was linked to a quadrupole mass spectrometer (QMS), NETZSCH QMS 403 *Aëolos*® Quadro, to detect and identify the gases during the decomposition of ~10 mg of CC-N-1:1:1 while heating up from 40 to 900 °C at 20 K.min^{-1} under an Ar flow of 20 mL.min^{-1}. The QMS data were analysed using the mass spectrometry NIST database.[45]

Results and discussion

CO_2 sorption cycling capacity

The cycling performance of each sample was evaluated by measuring the sorption capacity over multiple CO_2 absorption (exothermic) and desorption (endothermic) cycles, to assess the stability of these systems for potential TCB applications. Figure 1a depicts the absorption capacity of the samples after 100 cycles at 750 °C of 1 h each step with desorption under vacuum and absorption at ~5 bar of CO_2, relative to the initial absorption capacity measured during the first absorption. This visualisation allows a direct comparison of the performance of each sample. The closer the circle is to the line, the better the retention of capacity. The horizontal position of the circle corresponds to the maximum sorption capacity, whereas the vertical position characterises the cyclic stability of the material. The circles are sized according to the maximum CO_2 wt.% calculated using the carbonate content in the sample, hence the bigger the circle, the more energy that can be stored through TCES in the material. Figure 1b shows the evolution of the CO_2 cyclic capacity over the 100 cycles. All samples underwent differing degrees of absorption capacity decreasing over 100 cycles, although reaching asymptotic capacities. BM-AC-1:1:1 was an exception as the capacity increased by 17% over the 100 cycles compared to its first CO_2 absorption. The natural ankerite samples had the lowest initial capacity, which decreased drastically and rapidly during the first ten cycles, behaving in a similar manner to pure $CaCO_3$.[8] Higher contents of Mg and Fe enhanced the reversible CO_2 sorption, in fact samples with a
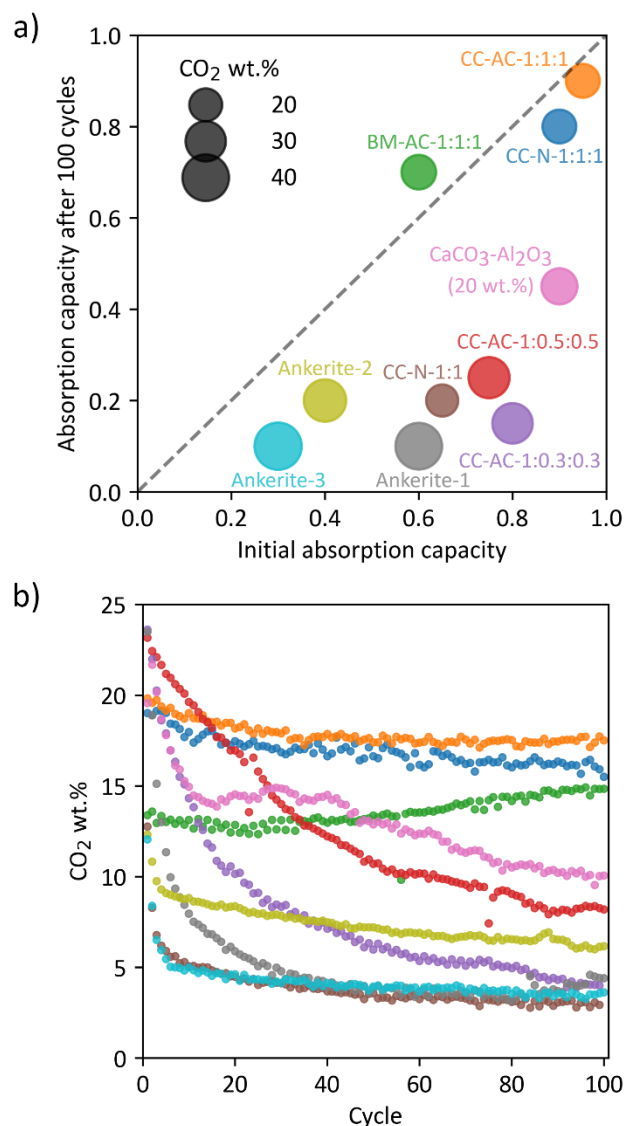

Figure 1. (a) CO_2 absorption capacity of the natural ankerite and the synthetic Ca-Mg-Fe composites after 100 cycles at 750 °C with 1 h desorption under vacuum and 1 h absorption at 5 bar of CO_2, relative to the initial absorption capacity (first cycle). (b) Evolution of the corresponding cyclic CO_2 capacity over the 100 cycles. The colour codes referring to the annotated materials in (a) are identical in (b).

Ca:Mg:Fe ratio of 1:1:1 showed a capacity of about 0.8, rather than 0.2 for ratios 1:0.5:0.5 and 1:0.3:0.3. The synthesised composite without Mg, CC-N-1:1, followed the decreasing trend of natural ankerite, and the final capacity was 0.2. Anwar *et al.* measured a similar conversion for their sample with a Ca:Fe ratio of 1:1 after 40 cycles.[36] Information on the reaction kinetics are available in Figure S1 (ESI). The evolution of the CO_2 absorption capacity over time during the first cycle shows fast absorption reaction kinetics for each sample, with the maximum reached within the first 5 min. Similar kinetic profiles are observed for each cycle, but for clarity only the first cycle is displayed.

The cycling data in Figure 1 allows us to compare the impact of different synthesis methods on performance. In fact, varying the precursors does not seem to greatly affect the cycling performance, with AC and N precursors resulting in samples

showing similar CO_2 capacity profiles after cycling but the CC-AC-1:1:1 sample has a slightly higher capacity. This minimal difference might have a significant impact on a larger scale system on long term utilisation. Also, it should be noted that the synthesis from nitrate precursors involves the release of NO_x, which is a highly toxic gas for human health and the environment.[46] Thus, AC precursors should be preferred for potential scale-up production of such composites. Regarding the synthesis process, the ball-milled sample required 'activation' before reaching maximum capacity (60+ cycles). Ball-milling may be more appealing than co-crystallisation for sustainable industrial production, but latency of the material activation would be a hindrance for TCES applications.[47] Interestingly, a previous cycling study of $CaCO_3$-Al_2O_3 (20 wt.%), maintained a CO_2 capacity of 0.6 over 400 cycles at 900 °C in similar cycling conditions.[8] Here, the capacity of the material dropped from 0.6 to 0.4 from the 50th cycle. Therefore, the lower temperature operation (750 °C) might affect the catalyst formation or activity in the $CaCO_3$-Al_2O_3 system. As such, XRD analyses before and after the cycling experiment (Table S2 and Figures S2-3-4, ESI) show a large proportion of unreacted Al_2O_3. Conversely, the Ca-Mg-Fe (1:1:1) composites demonstrated outstanding stability at 750 °C (e.g. 80 – 90%). Accordingly, the Ca-Mg-Fe (1:1:1) system appears to be a good candidate for TCB applications at more convenient operating conditions of pressure and temperature than the previously studied calcium carbonate systems.[11] Particularly, this enables lower temperatures than 900 °C (with absorption at 2 bar CO_2 for $CaCO_3$-Al_2O_3), and lower pressure than 30 bar (at 550 °C for a dolomite/molten salts composite).[8, 11, 12] Prior to implementation into TCB prototypes, it is crucial to understand the reaction mechanism of the TCES material, determine the physical properties, and assess the overall potential of the Ca-Mg-Fe system. The results of the cycling experiment show that: (i) the ratio 1:1:1 was the best performed samples, thus the presence of a significant amount of Mg- and Fe-bearing compounds must have an effect on the reversibility of the carbonation and prevent the sintering of the material; (ii) the synthesis process (e.g. ball milling) may affect the initial arrangement of the composite.

Phase composition

XRD and SR-XRD allowed for analysis of the composition of the samples at different stages of the CO_2 cycling experiments. The natural ankerite mineral samples contain various impurities that could not be identified in the refinement of the data. Thus, the corresponding composition results must be interpreted cautiously. Table S3 and Figure S5a (ESI) show the composition of the natural ankerite samples before the 100 cycles. Ankerite-1 and -3 seem to contain a large amount of ankerite (67 – 86 wt.%) with gypsum and quartz impurities, respectively. Ankerite-2 does not contain any mineral ankerite but is composed of calcite (56 wt.%) and goethite (iron oxide hydroxide, 44 wt.%).[48] Consequently, the Ankerite-2 sample has an inherently higher Fe content than the other two natural samples. Interestingly, Ankerite-2 showed a higher cycling capacity than Ankerite-1 and -3 samples. Thus, a higher Fe

content may enhance the reversibility of the carbonation. Table S4 and Figure S5b (ESI) present the composition of the natural ankerite samples after cycling (carbonated state), where it is clear that no ankerite has been reformed under these experimental conditions. The cycled samples are composed of $CaCO_3$ and various oxides. Cycled Ankerite-2, which did not contain Mg-bearing minerals initially, presents $CaCO_3$ along with a majority of dicalcium ferrite ($Ca_2Fe_2O_5$, 56 wt.%) and minor phases of unreacted CaO and magnetite (Fe_3O_4). Cycled Ankerite-3 is composed of approximately equal proportions of $CaCO_3$, $Ca_2Fe_2O_5$, SiO_2 and MgO, with traces of $MgFe_2O_4$. Magnesium ferrite is formed during the decarbonation of the (Fe,Mg)CO_3 part of ankerite that decomposes prior to the calcium carbonate.[22] In an earlier study of the thermal decomposition of ankerite-ferroan dolomites, Milodowski *et al.* identified the reaction between $CaCO_3$ and $MgFe_2O_4$ forming $Ca_2Fe_2O_5$ and MgO, which seems to explain the present observations.[23] Cycled Ankerite-1 has a majority of unreacted CaO and a large proportion of $CaMgO_2$, instead of calcium and magnesium ferrites, which can be explained by a negligibly low iron content in this sample. The XRD patterns with the associated refinements of natural ankerite samples are presented in Figures S6-11 (ESI).

Figure 2a presents the composition of the synthesised Ca-Mg-Fe composites in the carbonated state before cycling. The XRD
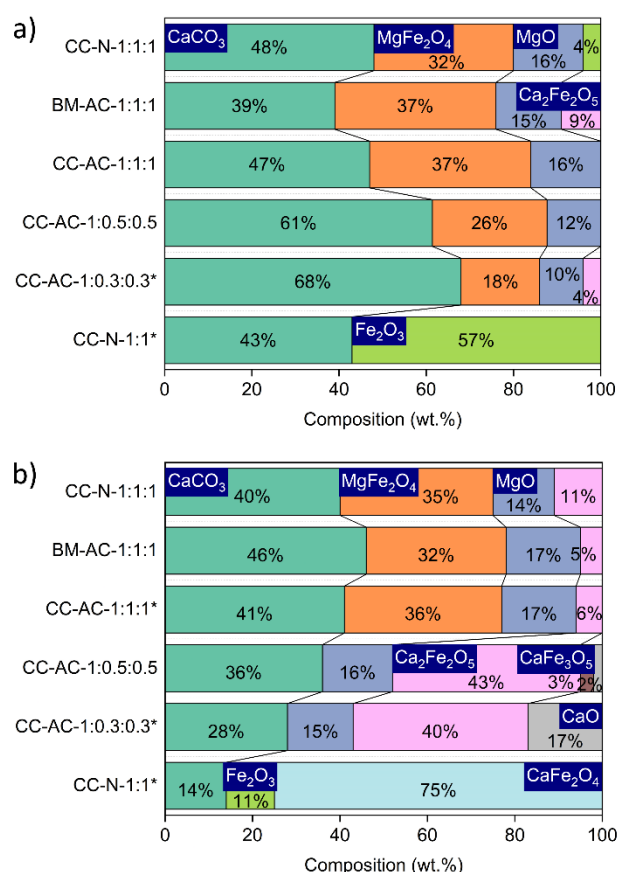
Figure 2. Composition of the samples (a) in the carbonated state before the cycling and (b) in the carbonated state after 100 cycles at 750 °C with 1 h vacuum desorption and 1 h absorption at 5 bar CO_2. Data are from SR-XRD except for samples marked with * which are XRD data collected using the Bruker D8D diffractometer.

patterns associated with the quantitative analysis (Tables S5-6, ESI) presented in Figure 2 are in Figures S12-23 (ESI). All the uncycled samples containing Mg consist of predominantly $CaCO_3$ (48 – 68 wt.%), magnesioferrite ($MgFe_2O_4$, 18 – 37 wt.%) and MgO (10 – 16 wt.%) with more or less $CaCO_3$ depending on the as-synthesised Ca:Mg ratio. CC-N-1:1 did not contain Mg and is therefore composed of only $CaCO_3$ (43 wt.%) and hematite (Fe_2O_3, 57 wt.%). The three different Ca:Mg:Fe (1:1:1) samples after cycling (Figure 2b) show a similar composition compared to their uncycled state, with less than 12 wt.% of $Ca_2Fe_2O_5$; while samples with less Mg/Fe are composed mostly of $Ca_2Fe_2O_5$, $\approx$ 15 wt.% of MgO, and unreacted CaO. Dicalcium ferrite results from a reaction between $CaCO_3$ and Fe_2O_3.[49, 50] In the case of CC-N-1:1, the main phase is $CaFe_2O_4$ with residual $CaCO_3$ and Fe_2O_3. Gao *et al.* studied the sintering process of hematite with CaO and showed that a stable phase of $CaFe_2O_4$ is forming by reaction between $Ca_2Fe_2O_5$ and Fe_2O_3 after long exposure at high temperature.[51] Thus, the stability of sintered $CaFe_2O_4$ probably explains the irreversible consumption of $CaCO_3$ preventing further carbonation in the case of sample CC-N-1:1.

The samples that showed the highest cycling performance: CC-N-1:1:1, BM-AC-1:1:1 and CC-AC-1:1:1, also show the presence of residual amounts of $Ca_2Fe_2O_5$, which seems to correlate with the capacity loss of these samples. Samples CC-AC-1:0.5:0.5 and CC-AC-1:0.3:0.3 initially contain a low proportion of $MgFe_2O_4$ and show a drastic drop in carbon dioxide sorption capacity during cycling. Importantly, magnesioferrite is absent in these samples at the end of cycling. Thus, the presence of $MgFe_2O_4$ must have a catalytic effect on the retention of the CO_2 sorption by the carbonate in the Ca-Mg-Fe system.

The composition of the samples with a Ca:Mg:Fe ratio of 1:1:1, which showed good cycling performance, were also analysed in their decarbonated state and compared to the initial and final carbonated states (Figure 2). In particular, Figure 3 compares the composition determined using Rietveld refinement of the XRD patterns of the different states of the CC-AC-1:1:1 sample, which demonstrated the best cycling performance.[41] CC-N-1:1:1 and BM-AC-1:1:1 showed similar compositions in each state (Figure S24, ESI), which suggests that these systems reacted

according to a similar reaction mechanism leading to a stable cycling capacity. Figures S25-27 (ESI) shows the SR-XRD patterns of the samples in the decarbonated state after the cycling.

The changes in composition observed between the decarbonated and carbonated states of the samples with a Ca:Mg:Fe ratio of 1:1:1 provide insight into the possible reaction mechanism. The main phases in the decarbonated sample are $Ca_2Fe_2O_5$ (42 wt.%) and MgO (21 wt.%), with similar amounts of $MgFe_2O_4$ (14 wt.%), CaO (12 wt.%) and magnetite (Fe_3O_4, 11 wt.%). Mass spectrometry analysis of the gas released upon decomposition of the carbonated material (Figure S28, ESI) confirmed that it is primarily CO_2 with a small amount of CO also detected when the CO_2 is desorbed. Hypothetically, a side reaction between CO_2 and iron oxide intermediates can occur, leading to the formation of Fe_3O_4 (change in the oxidation state of iron) and a CO/CO_2 gas phase.[49] The literature reports the utilisation of dicalcium ferrite in chemical looping for syngas production, acting as a catalyst oxygen carrier.[33, 34] Particularly, in certain conditions, the ferrite splits CO_2 inducing the formation of CO.[33]

$MgFe_2O_4$ and Fe_3O_4 have similar XRD patterns; therefore, the estimated quantification of each of these compounds in the samples may result in some innacuracy.[23] Milodowski *et al.* observed that $CaCO_3$ and $MgFe_2O_4$ are consumed to form $Ca_2Fe_2O_5$ and MgO during the decomposition of ferroan dolomites.[23] The associated reaction mechanism is likely to apply to the reversible sorption of CO_2 in the Ca:Mg:Fe composites synthesised in this study and is defined by eq. 5. According to this equation, the composition distribution should be 50 wt.% $CaCO_2$ and 50 wt.% $MgFe_2O_4$ in the carbonated state, then the decarbonation should yield 68 wt.% $Ca_2Fe_2O_5$, 10 wt.% MgO and 22 wt.% CO_2. Experimentally, the correct amount of carbon dioxide is desorbed from the system. The discrepancies observed in the amount of the other compound is due to the initial excess of Mg, preventing the decomposition of the magnesium ferrite, hence the formation of further dicalcium ferrite. The amount of carbonate could be maximised by optimising the ratio of Mg and Fe to avoid excessive compounds. The ideal ratio corresponding to eq. 5 is 1:0.5:1 of Ca:Mg:Fe.

$$2CaCO_3 + MgFe_2O_4 \rightleftharpoons Ca_2Fe_2O_5 + MgO + 2CO_2 \qquad (5)$$
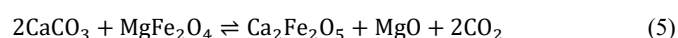
$MgFe_2O_4$ resides in a spinel structure, evolving towards a disordered configuration at temperatures higher than 550 °C.[52, 53] The reversible carbonation of the system may rely on the phase stability of $2CaO \cdot Fe_2O_3 \cdot MgO$ under different experimental condition of pressure and temperature, which may promote the formation of either magnesioferrite (eq. 6) or dicalcium ferrite (eq. 7).

$$MgFe_2O_4 \rightleftharpoons MgO + Fe_2O_3 \qquad (6)$$

$$2CaO + Fe_2O_3 \rightleftharpoons Ca_2Fe_2O_5 \qquad (7)$$

MgO and $MgFe_2O_4$ can co-exist in a solid solution and the formation of magnesioferrite depends on the concentration of Fe_2O_3.[54] Also, the formation of $MgFe_2O_4$ has been observed at high temperature when MgO is in contact with the calcium
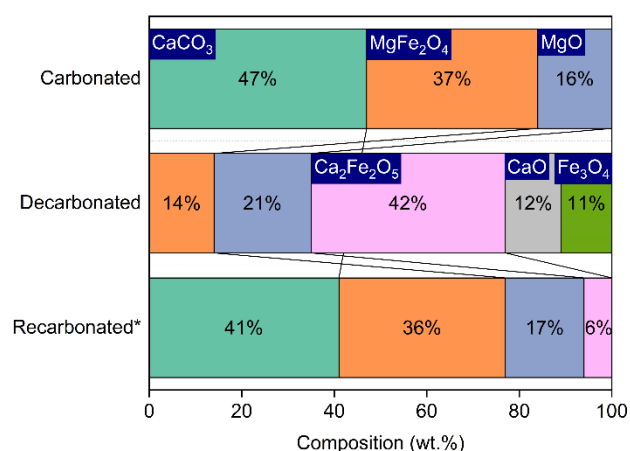

Figure 3. Composition of the CC-AC-1:1:1 sample in different states: initial carbonated, decarbonated and recarbonated after 100 cycles at 750 °C with 1 h vacuum desorption and 1 h absorption at 5 bar CO_2.

ferrite phase.[55] Jacob *et al.* determined the thermodynamics of eq. 7 to be $\Delta H = -45$ kJ.mol^{-1} and $\Delta S = 14$ J.mol^{-1}.K^{-1}.[56] Jeon *et al.* studied the formation of $Ca_2Fe_2O_5$ from CaO and Fe_2O_3 using TGA, showing no weight change but a slight increase in temperature.[57] Fe_2O_3 seems to alternate between forming dicalcium ferrite in the decarbonated state and magnesioferrite in the carbonated state of the system. Wu *et al.* identified a synergistic effect of the Fe_2O_3-CaO-MgO ternary system, resulting in lowering the fusion temperature of coal ash slag, and highlighted the impact of the ratio of the different oxides on the ferrites formation mechanisms.[58] In this study, the low levels of CO_2 sorption capacity with Mg and Fe ratios of 0.5 and 0.3 could be explained by the lack of enough Fe_2O_3 to perform the synergistic swing.

Thermodynamics

The determination of the thermodynamics of the reactions involved in the TCES system is crucial to assess the energy storage potential for applications. These thermodynamics of reaction (enthalpy and entropy) can be determined experimentally for solid-gas reactions through isothermal measurements in a manometric Sieverts-type apparatus, denoted pressure-composition-isotherms. The absorption PCI measurements are undertaken through step-wise CO_2 pressure increases at each temperature from vacuum. The CO_2 absorption PCI measurements of decarbonated CC-N-1:1:1 and the resulting van't Hoff plot are depicted in Figure 4. The absorption plateau elongates as temperature increases, with a maximum of ~18 wt.% CO_2 at 790 °C, whereas the CO_2 absorption reached ~24 wt.% at 880 °C. Also, at the highest temperature, absorption up to ~3 wt.% is noticeable at a pressure > 1 bar. The low pressure absorption is not observable at lower temperature. Thus, the absorption at low pressure and high temperature might correspond to a slow carbonation of CaO present in the sample. The enthalpy and entropy calculated from the pressure points in the CO_2 absorption plateau are $\Delta H_{abs} = -146 \pm 5$ kJ.mol^{-1} and $\Delta S_{abs} = -141 \pm 5$ J.mol^{-1}.K^{-1}.

In a similar manner, the CO_2 desorption PCI measurements and the resulting van't Hoff plots are depicted in Figure 5. The desorption PCI measurements are undertaken through step-wise CO_2 pressure decreases at each temperature from around 10 bar. The CO_2 wt.% increase at the start of the PCI measurements depicted in Figure 5a can be attributed to residual carbonations of the system at high pressure. Then, once the equilibrium is reached, decarbonation occurs. Also, the precision of the pressure gauge ($\pm 0.035/0 - 55$ bar) can slightly influence the CO_2 capacity measured, which is considered when determining the uncertainty of the thermodynamic calculations (Figure 5b). In Figure 5a, two plateaus are noticeable, suggesting that the CO_2 desorption reaction occurs in two steps. The main plateau at high CO_2 pressure accounts for about 18 wt.% of CO_2, while the low pressure plateau covers the remaining CO_2 desorption to a maximum of ~24 wt.%. The lower the temperature, the longer the low pressure plateau. This second step at low pressure might explain what was described at high temperature in the absorption PCI. The calculated thermodynamics for the high and
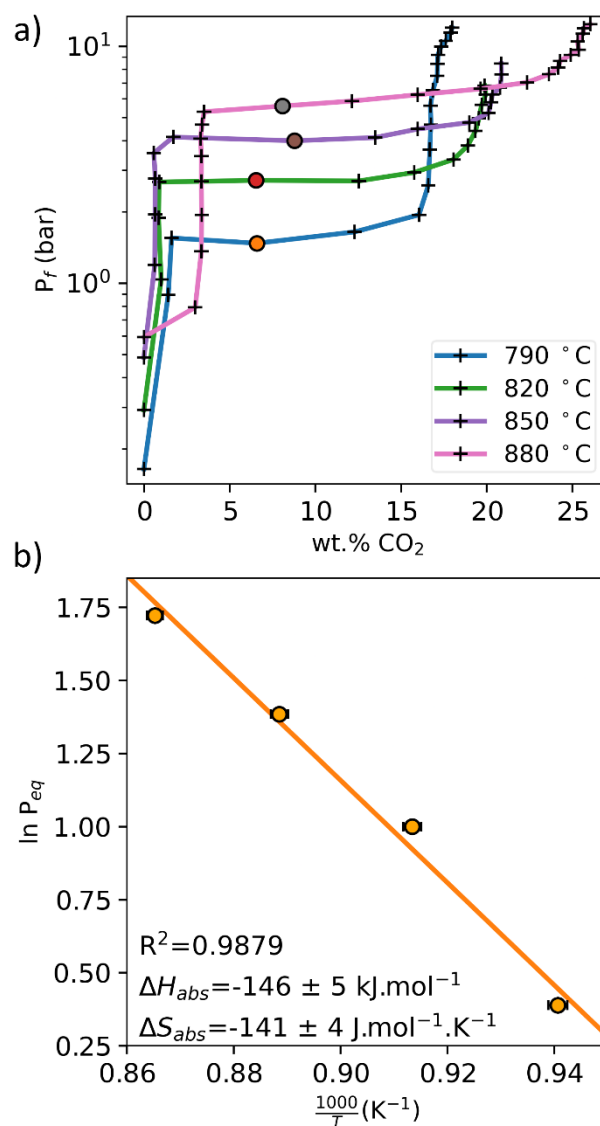

Figure 4. (a) CO_2 absorption PCI of decarbonated CC-N-1:1:1, where the coloured dots are the points chosen to get the equilibrium pressure values for each isotherm, and (b) the resulting van't Hoff plot used to determine the thermodynamics of the reaction.

low pressure plateaus are $\Delta H_{desHP} = 178 \pm 4$ kJ.mol^{-1}, $\Delta S_{desHP} = 167 \pm 4$ J.mol^{-1}.K^{-1} and $\Delta H_{desLP} = 178 \pm 5$ kJ.mol^{-1}, $\Delta S_{desLP} = 150 \pm 5$ J.mol^{-1}.K^{-1}, respectively. The reaction enthalpies of both steps are the same; however, the entropy is higher for the high pressure step. According to the composition of the system in the carbonated and decarbonated states (Figure 3), the high pressure plateau seems to correspond to the carbonation of the dicalcium ferrite. The equilibrium temperature at 1 bar of the low pressure plateau is 913 °C, which correlates with the 903 °C experimentally measured for the decarbonation of pure $CaCO_3$ by Desage *et al.* in a previous work.[11] Thus, the low pressure plateau seems to correspond to the decarbonation of $CaCO_3$ to form CaO. The absorption PCI measurement at low pressure and high temperature also show that CaO might be carbonated. The material must be isolated and analysed at this stage to confirm this hypothesis.

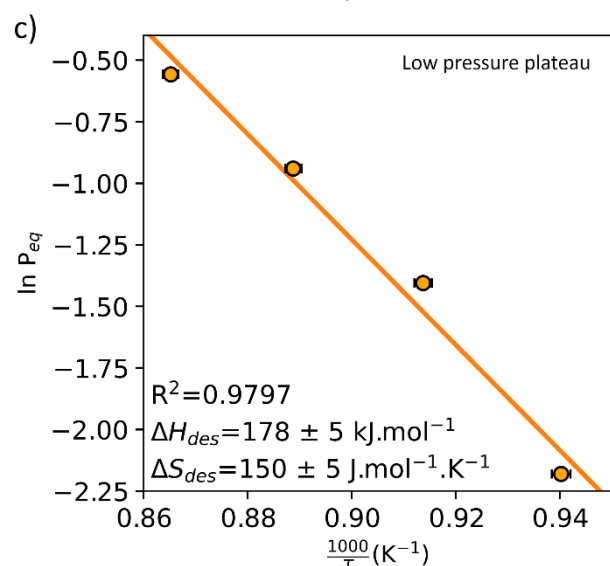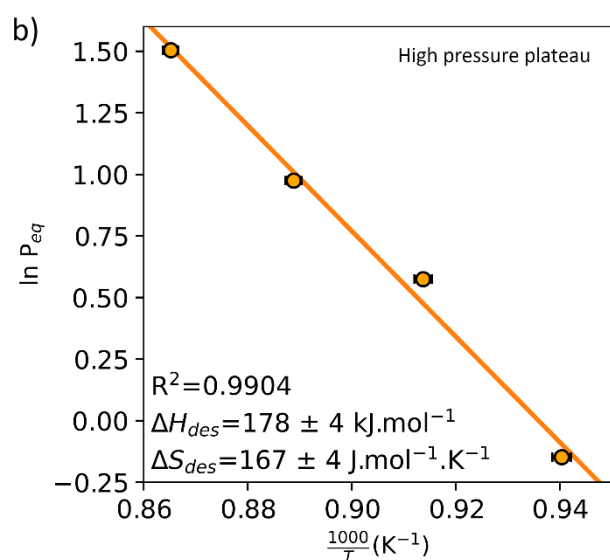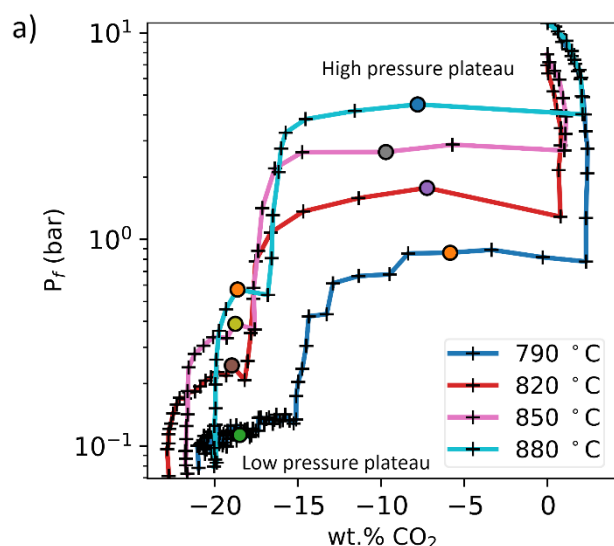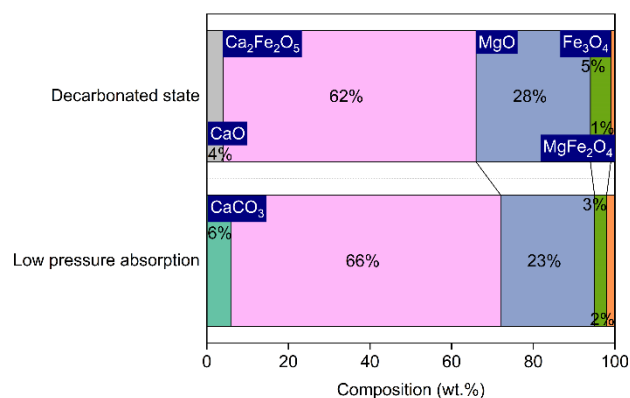The low pressure step was isolated by carrying out CO_2

Figure 6. Composition of sample CC-N-1:1:1 after absorption at low pressure (< 1 bar CO_2) at 820 °C compared to the composition of sample CC-N-1:1:1 in the fully decarbonated state.

Figure 5. (a) CO_2 desorption PCI of CC-N-1:1:1 in the carbonated state, where the coloured markers are the points chosen for the equilibrium pressure values for each isotherm, and the resulting van't Hoff plots used to determine the thermodynamics of the reaction for (b) the high pressure plateau, and (c) the low pressure plateau.

absorption for 1 h at 820 °C at a partial pressure of < 1 bar CO_2 in the Sieverts rig (Figure S29, ESI). The composition of the low pressure absorption isolated step is compared to the composition of the sample at the end of the desorption PCI measurement at 880 °C in Figure 6. The corresponding XRD patterns are available in Figures S30-31 (ESI). In the decarbonated state, the sample contains a majority of dicalcium ferrite (> 60 wt.%), ≈ 25 wt.% of MgO and 4 wt.% of CaO. The presence of Fe_3O_4 (5 wt.%) can be attributed to the side reaction mentioned earlier in the manuscript.[49] The sample absorbed ~2 wt.% of CO_2 (Figure S29, ESI) in 1 h at a partial pressure of CO_2 < 1 bar, resulting in the presence of 6 wt.% of $CaCO_3$ in at the end of the experiment, and CaO is not present anymore. The rest of the sample is composed of $Ca_2Fe_2O_5$ and MgO. These conditions of pressure and temperature are not favourable to the carbonation of the dicalcium ferrite nor to the reaction of MgO and Fe_2O_3 to form magnesioferrite.[32, 59] These observations suggest that the isolated low pressure plateau corresponds to the decomposition of excess $CaCO_3$ to CaO that does not react with Fe_2O_3 to form dicalcium ferrite. Thus, the thermodynamics of the low pressure plateau must correspond to those of the decomposition of pure calcium carbonate. These observations confirm that the main carbonation reaction (high pressure plateau) is driven by the synergistic swing of Fe_2O_3 to form either dicalcium or magnesium ferrites, which is temperature- and pressure-dependent. To summarise, both plateaus correspond to the decarbonation reaction of calcium carbonate, hence, the same enthalpy values. However, the entropy difference between the two reactions emphasises a difference in disorder between the solid phases. The hypothesis explaining why two steps are observed is the underlying formation of dicalcium ferrite in the case of the higher pressure step, while the lower pressure step results in the formation of residual CaO. Therefore, the synergistic decomposition of magnesium ferrite allowing for the formation of dicalcium upon the decarbonation of $CaCO_3$ shifts the reaction equilibrium pressure.

Figure 7 depicts an equilibrium diagram using the measured thermodynamics. The calcination enthalpy and entropy of $CaCO_3$, respectively 172 ± 8 kJ.mol^{-1} and 146 ± 7 J.mol^{-1}.K^{-1}, calculated in a previous work were used to show the desorption
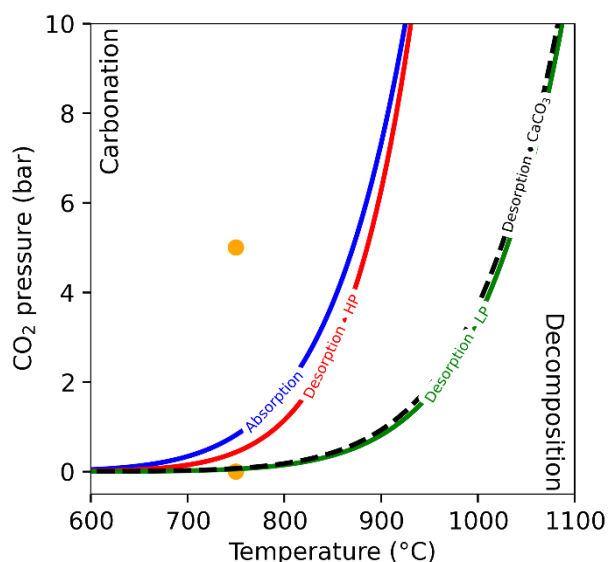
Figure 7. CO_2 equilibrium diagram of the Ca:Mg:Fe system 1:1:1 showing the curves for absorption and high and low pressure desorption steps calculated from measured thermodynamics. The desorption curve of pure $CaCO_3$ is also shown for comparison.[11] The orange dots show the cycling conditions of the system for absorption (5 bar CO_2) and desorption (vacuum).
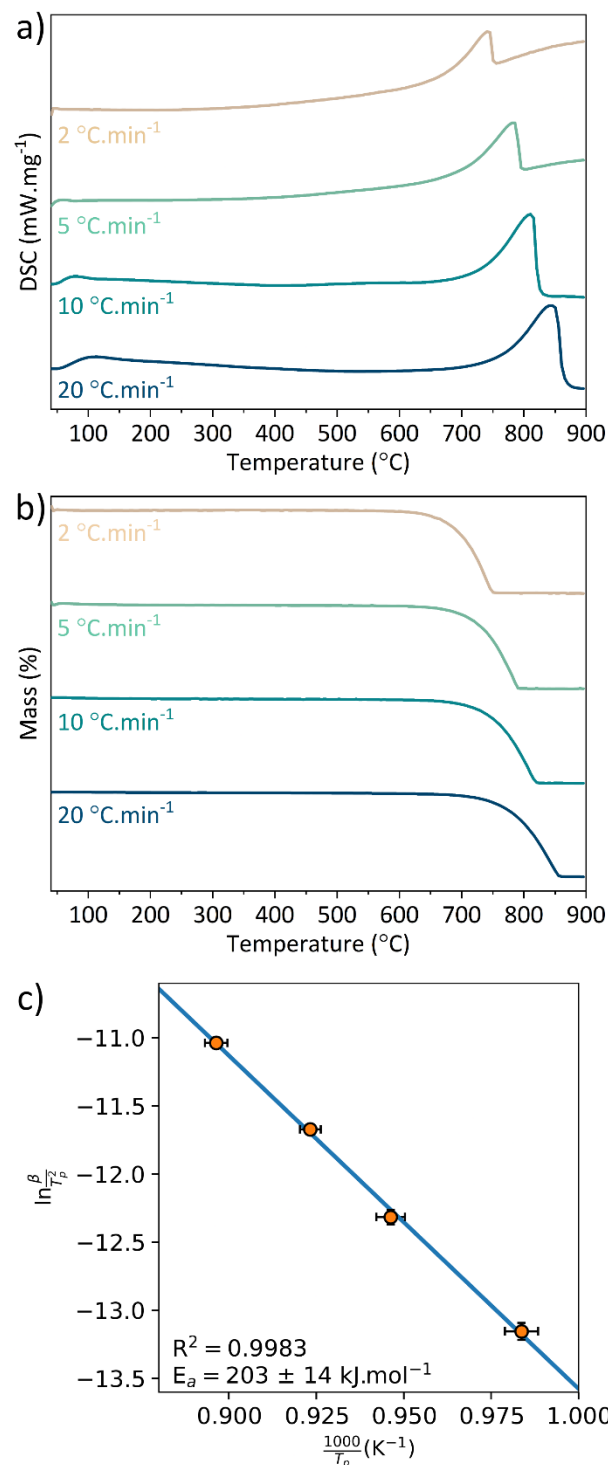

Figure 8. (a) DSC and (b) TGA signals at heating rates: 2, 5, 10 and 20 °C.min⁻¹. (c) Kissinger plot to determine the activation energy of the carbon dioxide desorption in the Ca:Mg:Fe (1:1:1) system (CC-N-1:1:1 sample).

equilibrium curve of pure $CaCO_3$.[11] Ismail *et al.* produced an equilibrium diagram for the carbonation of dicalcium ferrite.[32] The carbonation domain of the present system containing magnesium is shifted toward higher temperatures compared to solely calcium ferrite; therefore, $MgFe_2O_4$/MgO allows for higher temperature operating conditions. The absorption and high pressure desorption curves for the Ca:Mg:Fe system are similar to each other, showing little hysteresis. The low pressure desorption curve superimposes the desorption curve of pure $CaCO_3$, whereas the high pressure step relates to the reversible carbonation of $Ca_2Fe_2O_5 \cdot MgO$. During pressure cycling, the experimental conditions of 5 bar CO_2 for the absorption and vacuum desorption allowed for the completion of both (high and low pressure) steps within 1 h.

Activation energy

The activation energy for decomposition of Ca:Mg:Fe 1:1:1 (sample CC-N-1:1:1) was determined using the Kissinger method. The DSC signals collected at heating rates of 2, 5, 10 and 20 °C.min⁻¹ are presented in Figure 8a and were used to get the respective peak temperatures for CO_2 release of 743.4, 783.6, 809.9 and 842.4 °C. The desorption of ~20 wt.% of CO_2 was confirmed at each of the heating rates by the corresponding TGA signals (Figure 8b). The resulting activation energy from the Kissinger plot in Figure 8c is 203 ± 14 kJ.mol⁻¹. Anwar *et al.* reported that a $Ca_2Fe_2O_5$ additive lowered the decomposition activation energy of limestone waste from 182.3 to 162.3 kJ.mol⁻¹.[36] $CaCO_3$-Al_2O_3 (20 wt.%) was also reported with an activation energy of 169 ± 17 kJ.mol⁻¹.[11] Here, the estimated activation energy is closer to the value of 206 kJ.mol⁻¹ calculated by Olszak-Humienik *et al.* for the decomposition of natural dolomites and the 234 kJ.mol⁻¹ by Ptáček *et al.* for thermal decomposition of ferroan dolomites in inert atmosphere.[24, 60] According to the observation described

earlier, the determination of the absorption activation energy of the Ca:Mg:Fe 1:1:1 system would require CO_2 partial pressure higher than 1 bar to allow for the complete carbonation of the system.

Reaction pathways

The determination of the physical properties of the Ca:Mg:Fe 1:1:1 system, i.e. the sorption thermodynamics and the
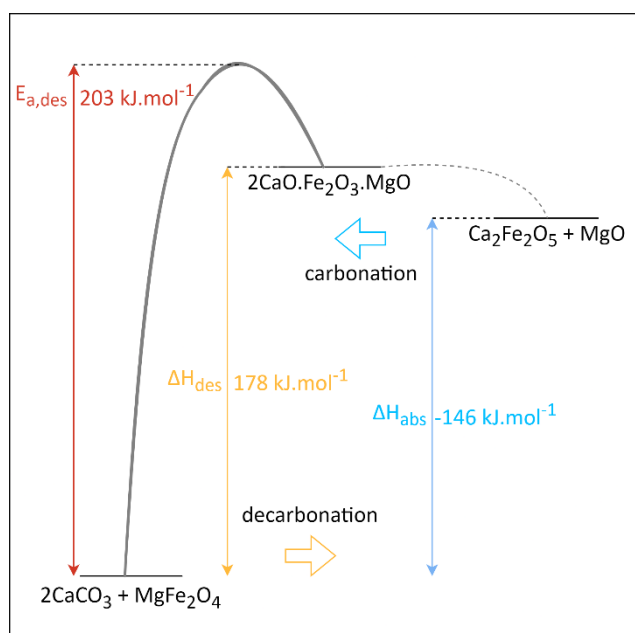
Figure 9. Inferred energy diagram for the reversible sorption of carbon dioxide in the intermediate compound $2CaO \cdot Fe_2O_3 \cdot MgO$.

desorption activation energy, suggest the energy diagram presented in Figure 9 to describe the reactions pathways. As mentioned earlier, $MgFe_2O_4$ co-exists in solid solution with MgO and Fe_2O_3 ($Fe_2O_3 \cdot MgO$).[54] Upon desorption, CaO produced from the decarbonation of $CaCO_3$ reacts with $Fe_2O_3 \cdot MgO$ in a slightly exothermic reaction leading to $Ca_2Fe_2O_5$ and MgO, as seen by XRD.[56, 57] Thus, the formation of the $2CaO \cdot Fe_2O_3 \cdot MgO$ intermediate is suggested because excess of each member of this complex were observed in the decarbonated state. Inversely, the absorption of CO_2 by the dicalcium ferrite forms $CaCO_3$ while MgO reacts with the released Fe_2O_3 to form magnesioferrite, also seen by XRD.[55] Overall, the Fe_2O_3 acts synergistically in the $2CaO \cdot Fe_2O_3 \cdot MgO$ system by forming either of the Ca and Mg ferrites, promoting the reversible sorption of carbon dioxide in the system.

Thermochemical battery implementation

The physical properties and cycling performance of Ca:Mg:Fe 1:1:1 emphasise the potential value of such TCES materials for implementation into TCBs. Effective cycling at 750 °C could be more preferrable from a technical standpoint compared to the 900 °C in typical $CaCO_3$ systems.[8, 13, 61] Operating at 750 °C allows for overcoming the challenges of high-temperature systems identified in a recently published review article.[7] Also, the optimal operating temperature of a large-scale Stirling engine (40 kW) is about 700 °C; therefore, the Ca:Mg:Fe system is a suitable TCES material for applications using a heat-to-power engine, such as a TCB.[7, 11] Considering −146 kJ.mol⁻¹, the enthalpy of the exothermic absorption of CO_2 in the $2CaO \cdot Fe_2O_3 \cdot MgO$, and 312 g.mol⁻¹ the molar mass of the material, the maximum energy density of the system is 468 kJ.kg⁻¹. Taking into account the stable capacity over cycles to be 0.9, this value drops to 421 kJ.kg⁻¹, which is nearly the double of the energy density of pure $CaCO_3$ system, which has a capacity drop to 0.15 over time (249 kJ.kg⁻¹).[7, 61] The maximum

energy density of $CaCO_3$-Al_2O_3 (20 wt.%) is 782 kJ.mol⁻¹.[8] However, the cycling of $CaCO_3$-Al_2O_3 (20 wt.%) at 750 °C showed a capacity drop to 0.4 in this work, resulting in an effective energy density of 313 kJ.kg⁻¹. Thus, at 750 °C the Ca:Mg:Fe system has a higher energy storage density. Optimising the metal ratios can maximise the energy storage density potential of the system. According to the mechanism identified and the residual iron oxides observed, an optimal ratio of Ca:Mg:Fe could be 1:0.5:1. The synthesis pathways presented in this study prove that the material can be easily prepared from cheap and abundant precursors, which is a tremendous advantage for the potential scale-up of this system. For example, considering a Ca:Mg:Fe optimal ratio of 1:0.5:1, the price of the TCES material can be estimated at \$0.75/kWh_th (using $CaCO_3$, MgO and Fe_2O_3 prices of respectively \$0.06, \$0.50 and \$0.75 per kg), which is nearly double of the \$0.33/kWh_th estimated for the $CaCO_3$-Al_2O_3 (20 wt.%).[8] However, the efficient operation of the Ca-Mg-Fe system at 750 °C is a significant asset in lowering the cost of the overall TCB; notably, by allowing for the integration of a cheaper heat transfer system compared to the possible options narrowed by the extremely high temperature required to operate $CaCO_3$-Al_2O_3 (< 950 °C).

The performance of the TCES material should now be assessed in a larger-scale TCB prototype and subjected to cost analysis would the results be promising. In addition, the extent of the side reactions releasing CO and its potential effect on the cycling capacity in a closed system must be investigated as it could be a limitation regarding the utilisation of this TCES material in a TCB. The carbonation state of the material is pressure/temperature driven; therefore, pressure/temperature swings are required to switch a TCB between charging and discharging modes. The energy penalty induced must be considered when evaluating the overall energy efficiency of the TCB.

Conclusions

This study characterised the Ca:Mg:Fe carbonate system as an innovative and efficient TCES material. Particularly, the samples synthesised via co-crystallisation of metal acetate precursors in a Ca:Mg:Fe ratio of 1:1:1 showed an outstanding CO_2 cycling capacity, with a retention of the CO_2 sorption to 90% of the maximum capacity over 100 cycles. XRD analysis allowed for the determination of the reaction mechanism, which involves the formation of $Ca_2Fe_2O_5$ during carbon dioxide desorption and the formation of $MgFe_2O_4$ during the absorption. The reaction pathway suggests that the swing of Fe_2O_3 to form the dicalcium or magnesium ferrites in the $2CaO \cdot Fe_2O_3 \cdot MgO$ system has a synergistic effect on the reversible sorption of carbon dioxide. The determination of the thermodynamics highlighted a pressure-temperature equilibrium different to that of pure calcium carbonate, particularly the system can operate at 750 °C with a pressure swing to < 1 bar CO_2 to trigger the decomposition and to 5 bar CO_2 to obtain the carbonation. The activation energy calculated for the decarbonation correlates with the values estimated for natural dolomites. Thanks to the experimental results of this study, the maximum energy density

of the system was estimated to be 468 kJ.kg^{-1}. This work presents valuable data to consider a scale-up of the system and assess the performance of the Ca:Mg:Fe system as a TCES material for TCB application. However, the mechanism synergism emphasised would require further analysis to optimise the ratio of metal to maximise the energy density while preserving the stability during cycling. In contrast to previous studies using dicalcium ferrite as an additive to limestone for TCES, the present work focused on the direct carbonation of $Ca_2Fe_2O_5$ and also involved magnesium ferrite in the reaction mechanism. Furthermore, the main asset of this Ca-Mg-Fe system is the lower operating temperature (750 °C compared to 900 °C for limestone systems), which can considerably reduce the thermal energy losses induced. While the proportion of ferrites is detrimental to the carbonate content conferring the energy storage density potential to the system, the outstanding stability of the CO_2 sorption capacity offered by the synergistic swing of the iron oxide to form the dicalcium and magnesium ferrites is crucial to ensure the reliability of the system implemented in power production plant at large scale.

Author contributions

Lucie Desage: Conceptualization, Data curation, Formal analysis, Investigation, Methodology, Writing - original draft, and Writing - review & editing **Terry D. Humphries:** Conceptualization, Data curation, Formal analysis, Funding acquisition, Investigation, Methodology, Project administration, Supervision, and Writing - review & editing **Mark Paskevicius:** Conceptualization, Data curation, Formal analysis, Funding acquisition, Investigation, Methodology, Project administration, Supervision, and Writing - review & editing **Craig E. Buckley:** Conceptualization, Funding acquisition, Project administration, Supervision, and Writing - review & editing

Conflicts of interest

The authors declare that they have no known competing financial interests or personal relationships that could appear to influence the work reported in this paper.

Acknowledgements

References

1   Intergovernmental Panel on Climate Change (IPCC), in Climate Change 2021 – The Physical Science Basis: Working Group I Contribution to the Sixth Assessment Report of the Intergovernmental Panel on Climate Change, Cambridge University Press, 2023, DOI: 10.1017/9781009157896.005, pp. 423-552.
2   C. A. Horowitz, International Legal Materials, 2016, **55**, 740-755.
3   Intergovernmental Panel on Climate Change (IPCC), Climate Change 2022 – Impacts, Adaptation and Vulnerability: Working Group II Contribution to the Sixth Assessment Report of the Intergovernmental Panel on Climate Change, Cambridge University Press, Cambridge, 2023.
4   S. Chu and A. Majumdar, Nature, 2012, **488**, 294-303.
5   K. M. Kennedy, T. H. Ruggles, K. Rinaldi, J. A. Dowling, L. Duan, K. Caldeira and N. S. Lewis, Advances in Applied Energy, 2022, **6**, 100091.
6   U. Pelay, L. Luo, Y. Fan, D. Stitou and M. Rood, Renewable and Sustainable Energy Reviews, 2017, **79**, 82-100.
7   L. Desage, E. McCabe, A. P. Vieira, T. D. Humphries, M. Paskevicius and C. E. Buckley, Journal of Energy Storage, 2023, **71**, 107901.
8   K. T. Møller, A. Ibrahim, C. E. Buckley and M. Paskevicius, Journal of Materials Chemistry A, 2020, **8**, 9646-9653.
9   J. Sunku Prasad, P. Muthukumar, F. Desai, D. N. Basu and M. M. Rahman, Applied Energy, 2019, **254**, 113733.
10 A. Reller, R. Emmenegger, C. Padeste and H.-R. Oswald, Chimia International Journal for Chemistry, 1991, **45**, 262-266.
11 L. Desage, T. D. Humphries, M. Paskevicius and C. E. Buckley, Journal of Energy Storage, 2024, **90**, 111917.
12 T. D. Humphries, K. T. Møller, W. D. A. Rickard, M. V. Sofianos, S. Liu, C. E. Buckley and M. Paskevicius, Journal of Materials Chemistry A, 2019, **7**, 1206-1215.
13 M. Benitez-Guerrero, B. Sarrion, A. Perejon, P. E. Sanchez-Jimenez, L. A. Perez-Maqueda and J. Manuel Valverde, Solar Energy Materials and Solar Cells, 2017, **168**, 14-21.
14 N. Amghar, P. E. Sánchez Jiménez, L. A. Pérez Maqueda and A. Perejón, Journal of Energy Storage, 2023, **63**, 106958.
15 S. Bai, J. Sun, L. Liu, Y. Da, Z. Zhou, R. Wang, Y. Guo and C. Zhao, Solar Energy Materials and Solar Cells, 2022, **239**, 111659.
16 Y. Da, Y. Xuan, L. Teng, K. Zhang, X. Liu and Y. Ding, Chemical Engineering Journal, 2020, **382**, 122815.
17 L. Yang, Z. Huang and G. Huang, Energy & Fuels, 2020, **34**, 11479-11488.
18 J. L. Kulp, P. Kent and P. F. Kerr, American Mineralogist, 1951, **36**, 643-670.
19 K. Iwafuchi, C. Watanabe and R. Otsuka, Thermochimica Acta, 1983, **66**, 105-125.
20 R. S. Arvidson and J. W. Morse, in Treatise on Geochemistry (Second Edition), eds. H. D. Holland and K. K. Turekian, Elsevier, Oxford, 2014, DOI: 10.1016/B978-0-08-095975-7.00703-8, ch. 9.3, pp. 61-101.
21 J. W. Anthony, R. A. Bideaux, K. W. Bladh and M. C. Nichols, Journal, 2001.
22 J. V. Dubrawski and S. S. J. Warne, Mineralogical Magazine, 1988, **52**, 627-635.
23 A. E. Milodowski, D. J. Morgan and S. S. J. Warne, Thermochimica Acta, 1989, **152**, 279-297.
24 P. Ptáček, F. Šoukal and T. Opravil, Solid State Sciences, 2021, **122**, 106778.
25 J. R. Goldsmith, D. L. Graf, J. Witters and D. A. Northrop, The Journal of Geology, 1962, **70**, 659-688.
26 S. S. J. Warne, D. J. Morgan and A. E. Milodowski, Thermochimica Acta, 1981, **51**, 105-111.

27 L. Chai and A. Navrotsky, Geochimica et Cosmochimica Acta, 1996, **60**, 4377-4383.

28 P. L. McSwiggen, Physics and Chemistry of Minerals, 1993, **20**, 42-55.

29 H. C. Gomes, S. S. Teixeira and M. P. F. Graça, Journal of Alloys and Compounds, 2022, **921**, 166026.

30 H. Qin, Y. He, P. Xu, D. Huang, Z. Wang, H. Wang, Z. Wang, Y. Zhao, Q. Tian and C. Wang, Advances in Colloid and Interface Science, 2021, **294**, 102486.

31 D. H. de Hoyos-Sifuentes, P. J. Reséndiz-Hernández, J. A. Díaz-Guillén, R. M. Ochoa-Palacios and G. Altamirano-Guerrero, Journal of Materials Research and Technology, 2022, **18**, 3130-3142.

32 M. Ismail, W. Liu, M. S. C. Chan, M. T. Dunstan and S. A. Scott, Energy & Fuels 2016, **30**, 6220-6232.

33 M. S. Sukma, Y. Zheng, P. Hodgson and S. A. Scott, Energy & Fuels, 2022, **36**, 9410-9422.

34 Z. Sun, S. Chen, J. Hu, A. Chen, A. H. Rony, C. K. Russell, W. Xiang, M. Fan, M. Darby Dyar and E. C. Dklute, Applied Energy, 2018, **211**, 431-442.

35 Z. Sun, X. Wu, C. K. Russell, M. D. Dyar, E. C. Sklute, S. Toan, M. Fan, L. Duan and W. Xiang, Journal of Materials Chemistry A, 2019, **7**, 1216-1226.

36 R. Anwar, R. K. Vijayaraghavan, P. J. McNally, M. M. Dardavila, E. Voutsas and M. V. Sofianos, RSC Advances, 2023, **13**, 32523-32531.

37 D. A. Sheppard, M. Paskevicius, P. Javadian, I. J. Davies and C. E. Buckley, Journal of Alloys and Compounds, 2019, **787**, 1225-1237.

38 K. Williamson, A. D'Angelo, T. D. Humphries, M. Paskevicius and C. E. Buckley, Journal of Energy Storage, 2024, **86**, 111196.

39 K. S. Wallwork, B. J. Kennedy and D. Wang, Aip Conf Proc, 2007, **879**, 879.

40 B. Schmitt, C. Bronnimann, E. F. Eikenberry, F. Gozzo, C. Hormann, R. Horisberger and B. Patterson, Nucl Instrum Meth A, 2003, **501**, 267-272.

41 A. A. Coelho, Journal of Applied Crystallography, 2018, **51**, 210-218.

42 E. Lemmon, I. H. Bell, M. Huber and M. McLinden, Standard Reference Data Program, Gaithersburg, 2018.

43 T. Renner, Quantities, units and symbols in physical chemistry, The Royal Society of Chemistry, 2007.

44 H. E. Kissinger, Analytical chemistry, 1957, **29**, 1702-1706.

45 E. Sisco, A. S. Moorthy and L. M. Watt, Journal of the American Society for Mass Spectrometry, 2021, **32**, 685-689.

46 World Health Organization, Health aspects of air pollution with particulate matter, ozone and nitrogen dioxide: report on a WHO working group, Bonn, Germany 13-15 January 2003, Copenhagen: WHO Regional Office for Europe, 2003.

47 S. L. James, C. J. Adams, C. Bolm, D. Braga, P. Collier, T. Friščić, F. Grepioni, K. D. M. Harris, G. Hyett, W. Jones, A. Krebs, J. Mack, L. Maini, A. G. Orpen, I. P. Parkin, W. C. Shearouse, J. W. Steed and D. C. Waddell, Chemical Society Reviews, 2012, **41**, 413-447.

48 J. M. Bigham, R. W. Fitzpatrick and D. G. Schulze, Soil Science Society of America, 2018, DOI: 10.2136/sssabookser7.c10, pp. 323-366.

49 I. Antunes, L. C. M. Ruivo, L. A. C. Tarelho, A. A. Yaremchenko and J. R. Frade, Ceramics International, 2022, **48**, 34025-34032.

50 B. F. Amorim, M. A. Morales, F. Bohn, A. S. Carriço, S. N. de Medeiros and A. L. Dantas, Physica B: Condensed Matter, 2016, **488**, 43-48.

51 L. Gao, P. Liu, W. Zhan, J. Zhang, Z. He and X. Hou, Advanced Powder Technology, 2022, **33**, 103712.

52 D. Levy, V. Diella, M. Dapiaggi, A. Sani, M. Gemmi and A. Pavese, Physics and Chemistry of Minerals, 2004, **31**, 122-129.

53 A. E. Paladino, Journal of the American Ceramic Society, 1960, **43**, 183-191.

54 I.-H. Jung, S. A. Decterov and A. D. Pelton, Journal of Physics and Chemistry of Solids, 2004, **65**, 1683-1695.

55 S. Yan, S. Sun and S. Jahanshahi, Metallurgical and Materials Transactions B, 2005, **36**, 651-656.

56 K. Jacob, N. Dasgupta and Y. Waseda, Zeitschrift für Metallkunde, 1999, **90**, 486-490.

57 J.-W. Jeon, S.-M. Jung and Y. Sasaki, ISIJ International, 2010, **50**, 1064-1070.

58 H. Wu, J. Wang, X. Liu, X. Cao, Q. Guo and G. Yu, Fuel, 2023, **343**, 127963.

59 B. Jansi Rani, M. Durga, G. Ravi, P. Krishnaveni, V. Ganesh, S. Ravichandran and R. Yuvakkumar, Applied Physics A, 2018, **124**.

60 M. Olszak-Humienik and M. Jablonski, Journal of Thermal Analysis and Calorimetry, 2015, **119**, 2239-2248.

61 G. Grasa, B. González, M. Alonso and J. C. Abanades, Energy & Fuels, 2007, **21**, 3560-3562.